



## 저작자표시-비영리-변경금지 2.0 대한민국

이용자는 아래의 조건을 따르는 경우에 한하여 자유롭게

- 이 저작물을 복제, 배포, 전송, 전시, 공연 및 방송할 수 있습니다.

다음과 같은 조건을 따라야 합니다:



저작자표시. 귀하는 원저작자를 표시하여야 합니다.



비영리. 귀하는 이 저작물을 영리 목적으로 이용할 수 없습니다.



변경금지. 귀하는 이 저작물을 개작, 변형 또는 가공할 수 없습니다.

- 귀하는, 이 저작물의 재이용이나 배포의 경우, 이 저작물에 적용된 이용허락조건을 명확하게 나타내어야 합니다.
- 저작권자로부터 별도의 허가를 받으면 이러한 조건들은 적용되지 않습니다.

저작권법에 따른 이용자의 권리는 위의 내용에 의하여 영향을 받지 않습니다.

이것은 [이용허락규약\(Legal Code\)](#)을 이해하기 쉽게 요약한 것입니다.

[Disclaimer](#)

공학석사학위논문

**Fabrication of Highly Sensitive Flexible  
Nickel Oxide NTC Temperature Sensor using  
Monolithic Digital Laser Patterning Process**

모노리딕 디지털 레이저 패터닝 공정을 이용한 유연한  
고감도 니켈옥사이드 NTC 온도센서 제작

2019년 2월

서울대학교 대학원

기계항공공학부

정 부 성

# Abstract

Despite its high temperature-sensitivity and simple structure, negative temperature coefficient (NTC) thermistors have been limitedly adapted to artificial skin or epidermal temperature sensor due to its excessive processing temperature that is not compatible with flexible substrates. To address this, herein, we develop a low heat budget, single-step laser digital patterning process which enables monolithic integration of Ni-electrode and NiO-sensing channel under room-temperature ambient. Monolithically fabricated NiO NTC thermistor exhibits the highest temperature-sensing ability among reported NTC thermistors. (TCR  $-9.2\text{ }^{\circ}\text{C}^{-1}$ ,  $B=8162\text{ K}$  at  $25\text{ }^{\circ}\text{C}$ ) Physical analysis suggests that the superior temperature sensing ability originates from the unique thermal activation mechanism of the proposed process. Together with the superior temperature-sensitivity, low heat budget nature of the laser reductive sintering leads development of complete flexible temperature sensor array and conformally attachable temperature sensor. We believe that our demonstrations present great opportunities toward variable military applications such as artificial skin and epidermal temperature sensor by offering exceptionally simple yet effective laser thermal process.

**Keyword:** Laser digital patterning, Nickel oxide, temperature sensor, artificial skin, epidermal sensor

**Student Number:** 2017-24786

## Acknowledgement

저에게 온전한 2 년의 시간을 허락해 준 대한민국 육군 덕분에 이와 같은 연구를 수행할 수 있었습니다. 성실한 복무로 보답하겠습니다

위탁장교의 상황을 이해해주시고 많은 배려와 함께 연구를 올바른 방향으로 진행할 수 있도록 지도해 주신 고승환 교수님 감사드립니다.

백지와 같았던 저를 도와주시고, 이끌어주신 ANTS 의 모든 분들 감사합니다. 소중한 인연 잊지 않겠습니다.

언제나 버팀목이 되어주시는 아버지, 항상 저를 위해 기도해주시는 어머니와 동생, 가까이서 어려울 때마다 많은 도움 주셨던 장인어른과 장모님 감사드립니다.

마지막으로 언제나 저의 편이 되어주는 아내 임민지와 큰 행복을 주는 두 아이 서은, 지호에게 무한한 감사와 사랑을 전합니다.

2019년 2월

정 부 성

# Table of Contents

<b>Chapter 1. Introduction .....</b>	<b>1</b>
<b>Chapter 2. Experiment.....</b>	<b>4</b>
2.1 Preparation .....	4
2.2 Laser process.....	5
2.3 Measurement.....	7
2.3.1 Electrical resistance dependency on temperature .....	7
2.3.2 Characterization .....	7
<b>Chapter 3. Result &amp; Discussion .....</b>	<b>8</b>
3.1 Sensor performance .....	8
3.2 Raman spectroscopic study.....	11
3.3 XRD analysis .....	13
3.4 Internal structure change of NiO NP by laser process.....	15
3.5 Lowering $R_0$ by geometrical approach .....	17
3.6 Application.....	18
3.6.1 Artificial thermo-receptor array.....	18
3.6.2 Prosthetic hand.....	20
3.6.3 Respiration sensor.....	22
<b>Chapter 4. Conclusion.....</b>	<b>24</b>
<b>References.....</b>	<b>26</b>
<b>Abstract in Korean .....</b>	<b>31</b>

## List of Figures

**Figure 1** The schematic of NiO laser reductive sintering process.

**Figure 2** SEM images of (a) the pristine NiO NP layer and (b) the NiO sensing-channel after laser process

**Figure 3** (a) The electrical resistance dependency of Ni electrode and Ni-NiO-Ni structure on Temperature. (b) Fitting for material constant of thermistor (B-value). (c) Cycling test of NiO NTC thermistor. (d) Comparison of material constant of thermistor and highest process temperature with other reported NTC thermistors.

**Figure 4** (a) Raman spectrum of NiO NP film before (Pristine) and after (Sensor) laser process. The spectrum deconvolution of NiO-related Raman peaks near  $500\text{ cm}^{-1}$  (b) for pristine and (c) for sensing channel.

**Figure 5** (a) XRD spectrum of pristine NiO, low energy annealed NiO, Normal annealed NiO and bunsenite. (b) The zoomed image of NiO (111) peak and NiO (220) peak.

**Figure 6** The schematic of internal structure changes of NiO NP during laser process

**Figure 7** B value and electrical resistance to the increased effective width of the NiO sensing-channel with different geometric structures: (a) simulated and (b) experimental result

**Figure 8** (a) The 5x5 artificial thermo-receptor array (yellow circle: sensor), (inset)

optical microscope image of a single sensor. (b) Thermal image of masked IR irradiation on sensor array (c) Temperature mapping data acquired from the artificial thermo-receptor array.

**Figure 9** (a) The prosthetic hand covered with the temperature-sensible artificial skin. (red circle: sensor) (b) The experimental setting for water flow sensing. (c) Magnification image of the finger-tip sensor. (d) Sequential temperature measurement of each finger-tip sensors and thermal images (bottom) for the actual flow of the water.

**Figure 10** (a) Conformally attachable NiO epidermal temperature sensors attached on various facial positions. (b) Continuous monitoring of respiration temperature (c) Thermal images showing the temperature variation above upper-lip during respiration (d) Real-time monitoring of respiration temperature and SPO<sub>2</sub> change during the incremental exercise test (IET).

# Chapter 1. Introduction

An essential element of a successful military operation is to accomplish the mission while minimizing the casualties of combatants. Recently, the republic of Korea army is pursuing two improvement projects to minimize combatant losses: deploying robots performing risky missions and modernization of personal gears. If the robot can reproduce human sense of touch, it could perform delicate tasks<sup>1-5</sup> like dismantling improvised explosive devices (IEDs). Since the temperature sensing is a major touch sensing mechanism which delivers abundant information of touching object, the artificial skin with flexible temperature sensor system is an essential part of post military robots. Meanwhile, the modernization of personal gears allows the military commander to monitor the real-time status of the single combatant. By applying the epidermal temperature sensor, it is possible to automatically monitor the real-time status of the combatant, since temperature variation of our own body possesses significant physiological information about metabolic status of the human body.<sup>6,7</sup> Therefore, concept of continuous long-term monitoring of our body temperature via conformally attachable flexible temperature sensor provides great potential to combat force management.<sup>8,9</sup> In most cases of artificial skin and epidermal sensor, interested temperature variation remains only in a small change near the room temperature ( $\sim 30$  °C). For this reason, high temperature-sensitivity especially in a low temperature range is required to the flexible temperature sensors. Additionally, to ease the modulus matching with our



human body, the flexible temperature sensor is required to have low level of mechanical modulus.

To address these requirements, so far, majority of efforts have been focused on integrated circuit (IC) based temperature sensors.<sup>1,3,4,8</sup> Despite its high temperature-sensitivity and flexibility, however, complicated structure mostly accompanying multi-step photolithography process and resulting high manufacturing cost greatly hinders actual utilization of the IC temperature sensors. On the other hand, negative temperature coefficient (NTC) thermistor has clear advantage over the IC temperature sensor in that it exhibits much simple structure while shows equivalently high temperature-sensitivity.<sup>10</sup> However, the NTC thermistor also has the biggest challenge toward the actual utilization to the flexible temperature sensor. Since ceramics for majority of NTC thermistors require a high temperature annealing above 600 °C for forming or activation, that is not compatible with most flexible substrate and electrode,<sup>11,12</sup> further progress in thermistor type flexible temperature sensor has been substantially limited.

Meanwhile, laser direct writing (LDW) is an alternative patterning process by which various metallic and inorganic structures can be directly formed on various choices of substrates. Computer-aided digital patterning of LDW enables mask-less, vacuum-free and ultra-fast patterning process. One of the most distinct characteristic of LDW process is its low heat budget nature. By direct delivering marginal photothermal energy required for a specific thermal treatment, fast scanning of intensive laser irradiation enables selective thermal annealing while leaves no thermal damage on the substrates.<sup>13-16</sup> Owing to this, laser reductive

sintering (LRS), a sub-concept of LDW, has been successfully verified its potentials toward the flexible electronics. Especially, by reducing metal oxide nanoparticle (NP) immediately before the sintering stage, LRS successfully eliminates limitations originating from the easily oxidizing nature of metallic NPs and further expands the boundary of applicable metal to several transition metals.<sup>17-20</sup> We developed a simple yet novel laser process enabling monolithic integration of Ni-electrode and NiO-channel, which exhibits the highest temperature-sensitivity among other thermistor-based temperature sensors. The sensor system fabricated on flexible substrate is directly applicable to the temperature sensible artificial skin and epidermal temperature sensor.

## Chapter 2. Experiment

### 2.1 Preparation

Polyvinylpyrrolidone (PVP, Mw~10,000, Sigma-Aldrich) 1.458 g and 0.105 g of Hexadecyltrimethyl-ammonium bromide (CTAB, Sigma-Aldrich) are dissolved in 4.92 ml of 1-Pentanol (Sigma-Aldrich) using sonicator. After the dissolving, 6.72 g of Nickel Oxide nanoparticles (<50 nm, Sigma-Aldrich) are added and sonicated until the nanoparticles are completely dispersed.

Polyethyleneterephthalate (PET) thin film (25  $\mu\text{m}$ , 100  $\mu\text{m}$  thickness) is cleaned by deionized water with neutral detergent, and rinsed with Ethanol to eliminate surface-absorbed water molecules. The PET substrate is electrostatically attached to the slide glass (1 mm thickness, Fisherbrand) using corona treatment (High Frequency Generator, Electro-Technic Products) and fixed by cellophane tape. Corona treatment ensures conformal adhesion of PET film to the glass. Sufficient amount of NiO NP ink (>3 ml for 5 $\times$ 3 cm area) is spread onto the surface of the PET film and gently coated by the doctor blading technique. The cellophane tape attached along the edges of PET film also serves as a thickness-guiding wall for doctor blading process. Finally, coated NiO NP ink is dried under the atmospheric ambience for 1 hour to obtain uniform NiO film of 30  $\mu\text{m}$ -thick.

## 2.2 Laser process

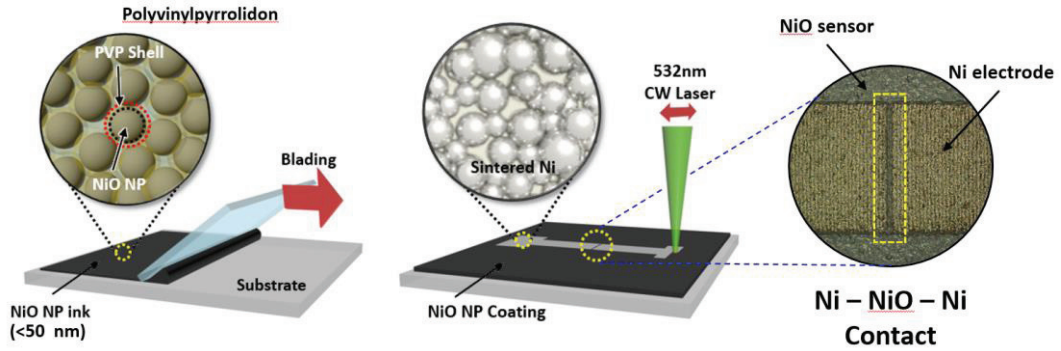


**Figure 1** The schematic of NiO laser reductive sintering process.

Figure 1 is a schematic of NiO LRS process. Before laser irradiation, it is believed that the NiO NPs are encapsulated by PVP molecules. When the laser irradiated on the NiO film, NiO NPs are reduced to Ni with the effect of reducing agent PVP and then sintered by photothermal treatment. Simultaneously, the laser irradiation induces the annealing and consolidation of the neighboring NiO NPs.

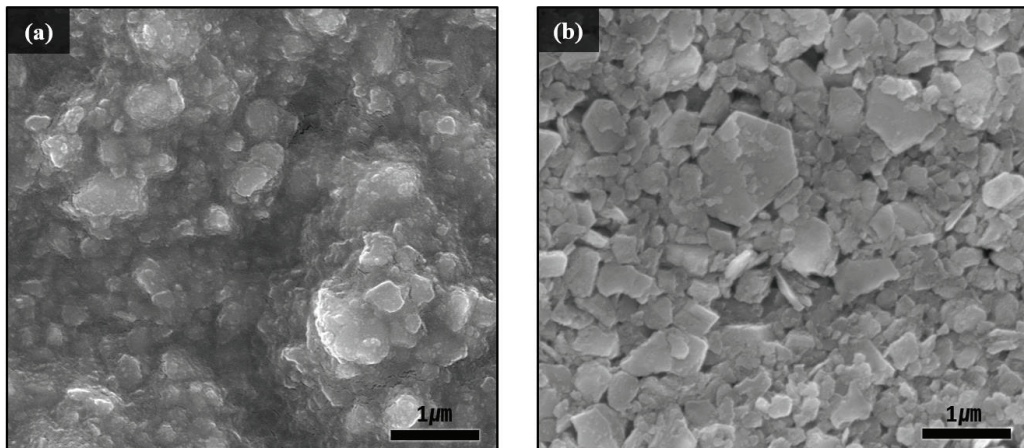


**Figure 2** SEM images of (a) the pristine NiO NP layer and (b) the NiO sensing-channel after laser process

Figure 2 shows the surface SEM images of NiO NP layer (2a) before and (2b) after the indirect laser thermal treatment. Organic materials, covering the surface of the pristine NiO NP layer, are no longer exist in the NiO sensing-channel. It suggests that the indirect laser irradiation could generate high temperature condition sufficient to decompose organic materials. Through a single monolithic laser process, a NiO sensor and a Ni electrode part with superior contact are fabricated concurrently from a single material. The visible laser at 532 nm wavelength (Sprout-G-5W, Lighthouse Photonics) is used as a heat source and the laser pattern, drawn by the CAD program, is scanned on the NiO film through a galvano-mirror scanner system (hurrySCAN II, Scanlab). The scanning speed and power of laser are basically 10 mm/s and 90 mW. The spacing between two adjacent scanning lines is set to be 30  $\mu\text{m}$  for the electrode part and 80  $\mu\text{m}$  for the sensing-channel. After laser scanning is completed, the substrate is cleaned with deionized water until the unnecessary parts are washed away. Through the DI water cleaning process, only laser treated part (Ni and heat treated NiO) remains on the PET substrate.

## **2.3 Measurement**

### **2.3.1 Electrical resistance dependency on temperature**

The electrical resistance was measured by the source measure unit (sourcemeter 2400, Keithley) and the temperature was controlled in range from 25 °C to 70 °C by data obtainable hot plate (MST-1000B, MS Tech). The temperature was elevated by 5 °C, and sufficient time was allowed to achieve thermal equilibrium state at each step. All measuring devices were installed inside the Faraday cage to minimize interference with other parameters except temperature.

### **2.3.2 Characterization**

The tendency in the crystallinity of the various NiO samples was compared by XRD analysis (D8-advanced, Bruker). The Raman spectroscopy (Horiba Jobin Yvon, LabRam Aramis) were obtained for crystalline characteristic analysis of pristine and laser treated NiO. The morphology of NiO NP layer was measured, before and after laser process, by field emission scanning electron microscopy (FE-SEM). The temperature images are captured to measure temperature distribution by an infrared (IR) camera (A645sc, FLIR systems). A Pulse Oxymetry (B370826886, DNV) was used to measure peripheral capillary oxygen saturation (SPO<sub>2</sub>) level.

# Chapter 3. Result & Discussion

## 3.1 Sensor performance

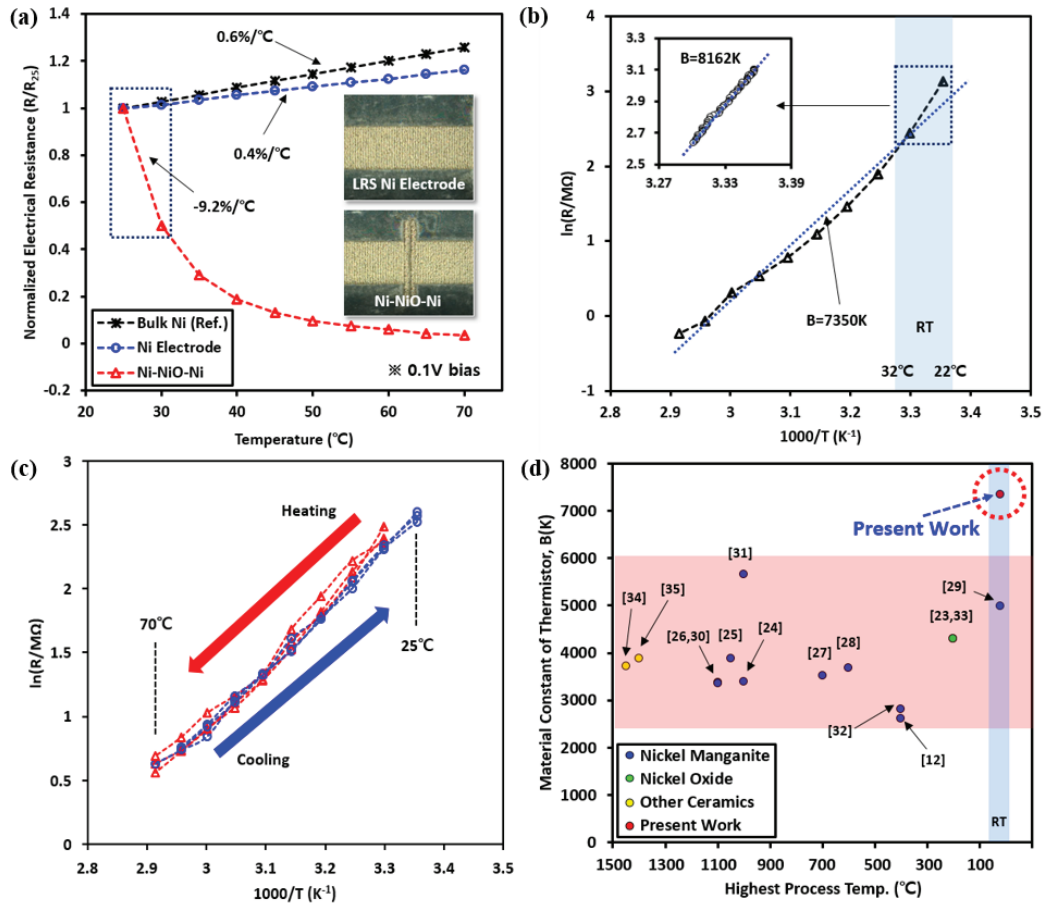


**Figure 3** (a) The electrical resistance dependency of Ni electrode and Ni-NiO-Ni structure on Temperature. (b) Fitting for material constant of thermistor (B-value). (c) Cycling test of NiO NTC thermistor. (d) Comparison of material constant of thermistor and highest process temperature with other reported NTC thermistors.

As presented in Figure 3a, Ni electrode and NiO sensor show contradictory

temperature coefficient of resistance (TCR). The electrical resistance of the NiO sensor drops dramatically between 25 and 70 °C. The significant decrease in resistance (TCR  $\sim -9.2$  %/°C) occurs between 25 and 30 °C. Conversely, the Ni electrode has positive temperature coefficient (TCR  $\sim 0.4$  %/°C), which is comparable to the property of bulk nickel. The overall electrical resistance property of the whole sensor system is determined by NiO sensor because of its overwhelmingly high resistance and TCR than Ni electrode. Through remarkably simple monolithic laser process, both metal electrode part and metal oxide sensor part with completely opposite electrical characteristics were fabricated. Also, the remarkable difference in TCR ensures that Ni electrode does not affect the temperature-sensitivity of the NiO sensor. In addition, despite the low driving voltage of 0.1 V, clean data was obtained as a result of the measurement.

For thermistor device with fixed dimensions and resistivity, the electrical resistance can be expressed as:

$$R(T) = R_{\infty} \exp(B/T) \quad (1)$$

Where  $R_{\infty}$  is the resistance of the thermistor at infinite temperature and  $B$  and  $T$  are the material constant of a thermistor and temperature respectively.<sup>10</sup> Commercial NTC thermistors have a  $B$  value ranging from 2000 and 5000 K at room temperature. As shown in figure 3b, Our NiO sensor have a remarkably high  $B$  value of 7350 K between 25 and 70 °C and 8162 K between 25 and 30 °C. To evaluate the reliability of the sensor, cycling test was conducted in the temperature range from 25 °C to 70 °C. Figure 3c shows that the NiO temperature sensor has high level of reliability



under three repetitions of test. Figure 3d shows comparison of the B value and the highest process temperature of the NTC thermistors reported in recently reported NTC thermistors.<sup>12,21-33</sup> The process temperature is an important factor to flexible temperature sensor research due to its compatibility with flexible substrates. Our present work has the highest B value while being fabricated at the lowest temperature of room temperature. Most NTC thermistors, using ceramics as sensing material, require high process temperatures to form or activate ceramics. Conventional bulk heating method is not compatible with thermally-vulnerable thin polymer substrates because it requires high temperature condition with long time. Since the laser could heat the target materials locally and sequentially, the heat damage of the substrate is significantly lower than that of the conventional bulk heating. Our present work is compatible with thin and flexible substrates through the low process temperature and certainly has high temperature-sensitivity.

### 3.2 Raman spectroscopic study

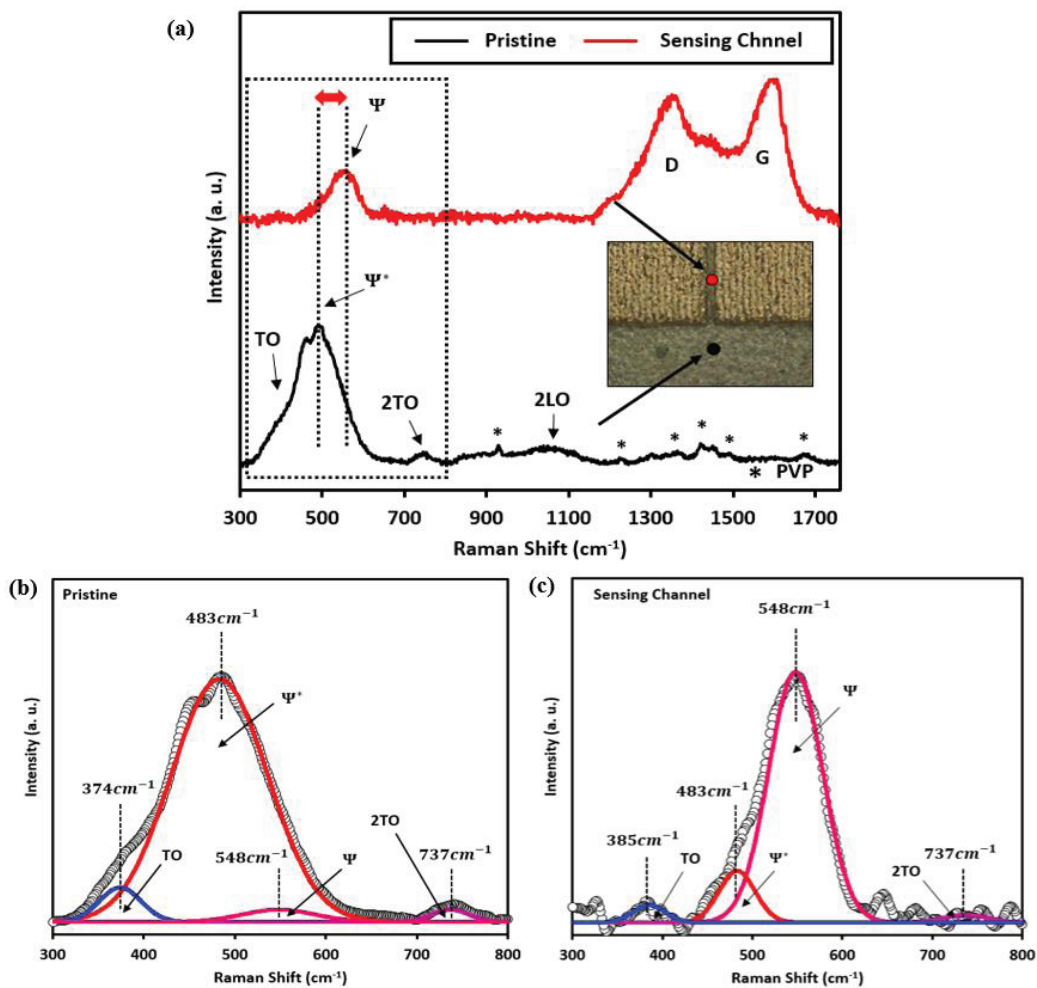


**Figure 4** (a) Raman spectrum of NiO NP film before (Pristine) and after (Sensor) laser process. The spectrum deconvolution of NiO-related Raman peaks near 500 $\text{cm}^{-1}$  (b) for pristine and (c) for sensing channel.

The Raman spectroscopic study was performed to confirm electrochemical changes

of NiO NPs after laser process. As shown in figure 4a, the PVP peak exhibited in the pristine sample disappears in the sensing channel sample, and the carbon D and G peak are grown instead. It means that the indirect laser irradiation could generate enough high temperature environment to cause carbonization of PVP without substrate damage. In addition, the decrease of innate crystalline defects of NiO NPs by laser process is expected. Figure 4a also shows a NiO-originated Raman peak (near  $500\text{cm}^{-1}$ ) shifts above the ordinary peak shift range after laser process. The deconvolution spectrum by Gaussian fitting confirms that the peak is consisted of three sub peaks, and the peak shift is caused by exhibition of peaks at  $480\text{ cm}^{-1}$  and  $550\text{ cm}^{-1}$  (figure 4b and 4c). According to previous research these peaks could be assigned to defect-rich NiO and stoichiometric NiO respectively.<sup>34,35</sup> Since the nickel vacancy is the major crystalline defect of NiO,<sup>36,37</sup> this result means that the laser process could make NiO NPs more stoichiometric by reducing innate nickel vacancies.

### 3.3 XRD analysis

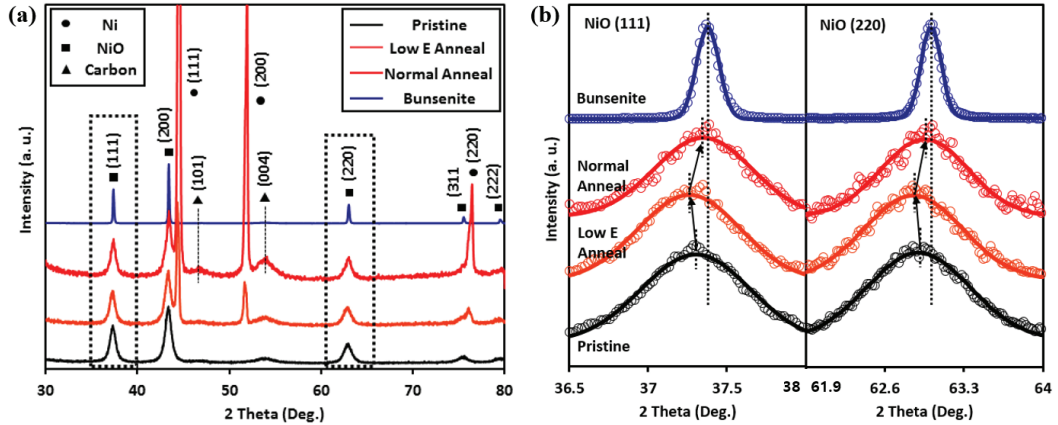


**Figure 5** (a) XRD spectrum of pristine NiO, low energy annealed NiO, Normal annealed NiO and bunsenite. (b) The zoomed image of NiO (111) peak and NiO (220) peak.

XRD analysis was performed to compare the lattice constant of various NiO samples. Figure 5a shows the result of four types of samples: bunsenite (single crystalline NiO), normal E anneal, low E anneal and pristine. The bunsenite sample used same fabrication process with pristine, only the NiO NP was replaced to green NiO powder (-325 mesh, Sigma-Aldrich). Normal annealing sample (45 J/m) and low energy annealing (30 J/m) sample are fabricated by producing different energy densities to pristine sample. Similar to the Raman spectroscopy result, carbon peaks are observed in the laser treated sample (normal anneal). By comparing two peaks (111, 220) among the identified NiO peaks, it is possible to deduce the mechanism of laser annealing process. As shown in figure 5b, both peaks are shifted to lower

angle in the low energy annealing phase and then shifted to higher angle (near bunsenite peak) in the normal annealing phase. The shift of the XRD peak to the higher angle means that the lattice constant decreases.<sup>36,38</sup> The crystal vacancies in ionic crystal induce lattice expansion, peak shift to higher angle implies decrease of crystalline vacancies in NiO NPs. As a result, the XRD analysis showed that the defect of NiO NPs increased when exposed to low power laser patterning, and then the defect decreased similar to stoichiometric NiO (bunsenite) when normal power laser was applied.

### 3.4 Internal structure change of NiO NP by laser process

The result of Raman spectroscopy and XRD analysis equally indicate that defect-rich NiO NPs become stoichiometric through the laser patterning process. The crystalline defect of NiO is mainly due to nickel vacancies but another type of defect (oxygen vacancy) is needed to explain opposite result of lowered laser power scanning sample. We proposed the internal structure change model of NiO NPs during laser process.

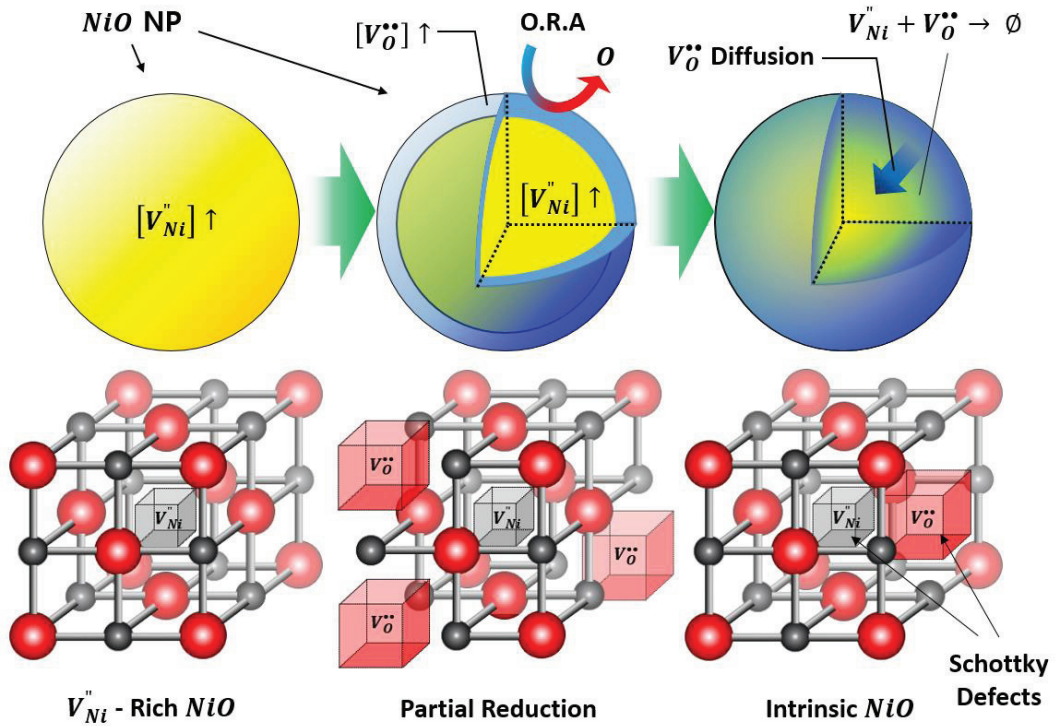


**Figure 6** The schematic of internal structure changes of NiO NP during laser process

As can be seen in figure 6, the pre-annealing NiO NPs are defect-rich and have a higher lattice constant than stoichiometric NiO. When thermal energy is applied, the organic reducing agent (ORA) is created by the thermal decomposition of PVP and forms a reducing environment. The oxygen vacancies generated at outer shell of NiO NPs and cause the lattice expansion by increasing the total vacancy. As a final step, when more thermal energy is applied, the oxygen vacancies are diffused to inside of lattice and combine with nickel vacancies by electrostatic attraction. The nickel vacancy and the Oxygen vacancy form a Schottky defect, which results the cancellation of the total vacancy, thus reducing the lattice constant.<sup>39</sup> Through the laser annealing process, the total vacancy was reduced and NiO NPs became more stoichiometric. This model could explain the origin of the superior temperature-sensitivity of the NiO temperature sensor. Previous studies have revealed that the decrease of nickel vacancies induces the increase of activation energy for the electrical conduction mechanism of NiO.<sup>40,41</sup> From the polaron hopping model of NiO electrical conduction, the electrical resistivity  $\rho$  of the NiO is expressed as:

$$\rho \sim \exp\left(\frac{E_a}{kT}\right) \quad (2)$$

where  $E_a$ ,  $k$  and  $T$  is the activation energy for electrical conductivity, the Boltzmann's constant and the temperature respectively.<sup>40</sup> From formula (1) and (2), it can be seen that  $E_a$  is proportional to the B value of thermistor. Thus, decreased nickel vacancy could explain the enhanced temperature-sensitivity of the NiO. As a result, our unique laser process could augment the temperature-sensitivity of the NiO temperature sensor without additional treatment.

### 3.5 Lowering $R_0$ by geometrical approach

Since the temperature-sensitivity of the NiO temperature sensor enhanced by increasing activation energy, the electrical resistance also increased after laser process. In most cases, high electrical resistance is an obstacle to the practical application of sensor networks.<sup>27</sup>

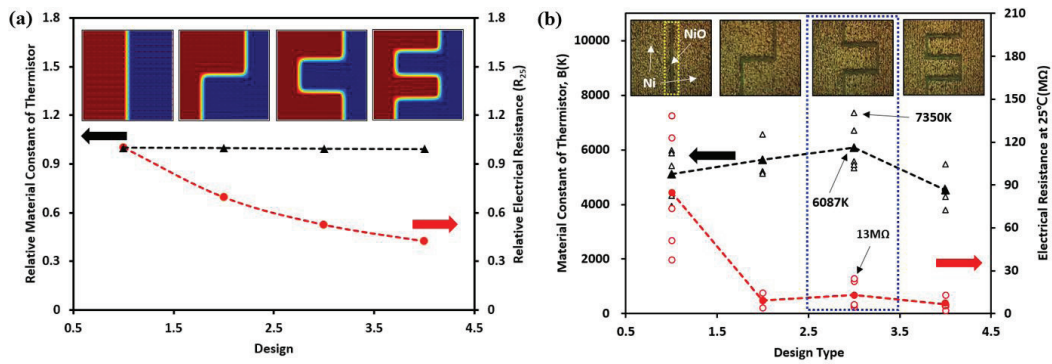


**Figure 7** B value and electrical resistance to the increased effective width of the NiO sensing-channel with different geometric structures: (a) simulated and (b) experimental result

As shown in figure 7, the effective width can be increased by changing the design of sensing-channel. Figure 7a shows the simulated result of sensitivity and electrical resistance of each design. The temperature-sensitivity is maintained while electrical resistance is decreasing. The design flexibility of the laser process allows each design to be applied without technical difficulties. As shown in figure 7b overall tendency of experimental result is similar with the simulated expectation, but the reduction of electrical resistance is more dramatic. Through the geometric approach, we could decrease the average electrical resistance to 10 % level, while maintaining high B value above 4000 K.



## 3.6 Application

### 3.6.1 Artificial thermo-receptor array

Techniques to fabricate high-performance temperature sensors on flexible substrates show the potential for use as artificial skin. A 5 x 5 artificial thermo-receptor array, for temperature-sensitive artificial skin, was designed by describing thermal receptors of the human skin. The matching of the temperature sensing range of the human skin's thermo-receptor and the range that our sensor can detect sensitively makes it possible to create a more human-like artificial thermo-receptor array.<sup>42</sup>

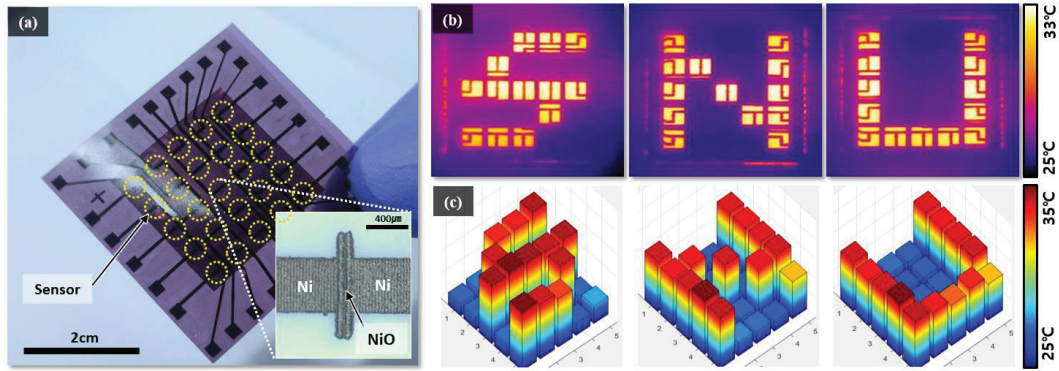


**Figure 8** (a) The 5x5 artificial thermo-receptor array (yellow circle: sensor), (inset) optical microscope image of a single sensor. (b) Thermal image of masked IR irradiation on sensor array (c) Temperature mapping data acquired from the artificial thermo-receptor array.

With a high design flexibility and monolithic process, 25 temperature sensors and read-out electrodes are simply manufactured on 100  $\mu\text{m}$  PET substrate (Figure 8a).

The spacing of each sensor is 5 mm, and each sensor with width of 1mm is connected by 0.5 mm wide electrodes. To verify the performance of the sensor array, we made an alphabetical aluminum mask and irradiated an IR light on the backside of the artificial thermo-receptor array to create a letter-shaped ('S', 'N' and 'U') temperature distribution. Figure 8b is a thermal image of the temperature distribution of the sensor array substrate taken with an infrared (IR) camera. As can be seen in figure 8c, the temperature distribution measured by the sensor array corresponds to the data of the substrate as determined by the IR camera.

### 3.6.2 Prosthetic hand

After confirming the feasibility of artificial thermo-receptor array for temperature-sensitive artificial skin, a prosthetic hand which can detect temperature was manufactured.

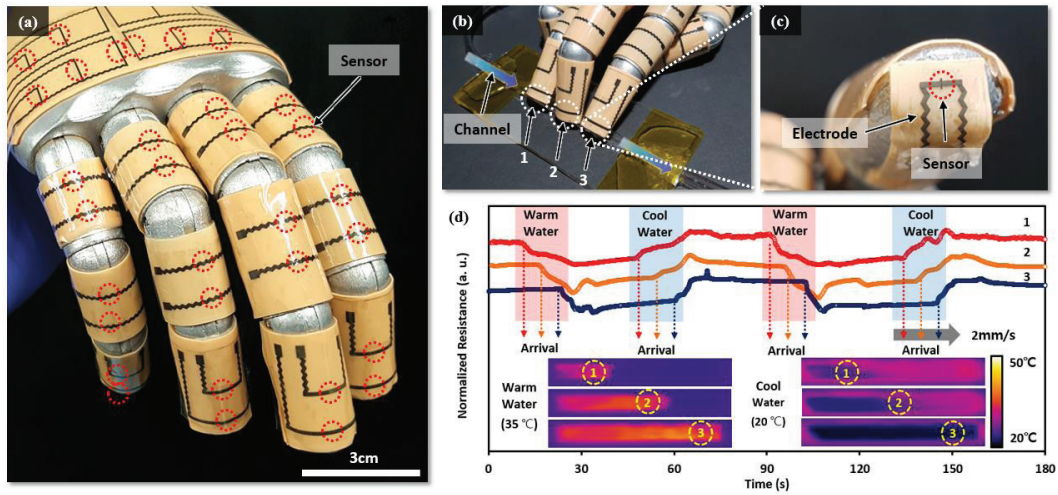


**Figure 9** (a) The prosthetic hand covered with the temperature-sensitive artificial skin. (red circle: sensor) (b) The experimental setting for water flow sensing. (c) Magnification image of the finger-tip sensor. (d) Sequential temperature measurement of each finger-tip sensors and thermal images (bottom) for the actual flow of the water.

Figure 9a shows the prosthetic hand covered with the temperature-sensitive artificial skin. Human skin was depicted with a 200  $\mu\text{m}$  thick elastomer (ecoflex 0030, smooth-on) on the model hand and the sensor was attached on it. Since the substrate is very thin and flexible (25  $\mu\text{m}$  PET), sensor could be attached to a curved elastomer surface only with the van der Waals force. The position of the sensor and

the shape of the electrode can be tailored to each part of the prosthetic hand by digital patterning. To demonstrate the sensing ability of the prosthetic hand, three finger-tip sensors are used to water flow sensing. Figure 9b and 9c show the experimental setting for water flow sensing and zoomed image of finger-tip sensor. Three fingers of the prosthetic hand are located on the polydimethylsiloxane (PDMS) channel in which warm (35 °C) and cool (20 °C) water are injected with the constant injection speed. Figure 9d shows the result data that provides the clear information about the detected temperature of injected water from three sensors. The electrical resistance of each sensors changes sequentially depending on the temperature of the water being injected. Since the spacing of the sensors is constant, it is possible to calculate the water injection speed (2 mm/s). These results verify a potential to practical use in artificial skin applications. With temperature-sensible artificial skin, robots can perform more delicate work by reproducing vivid human touch of sense.

### 3.6.3 Respiration sensor

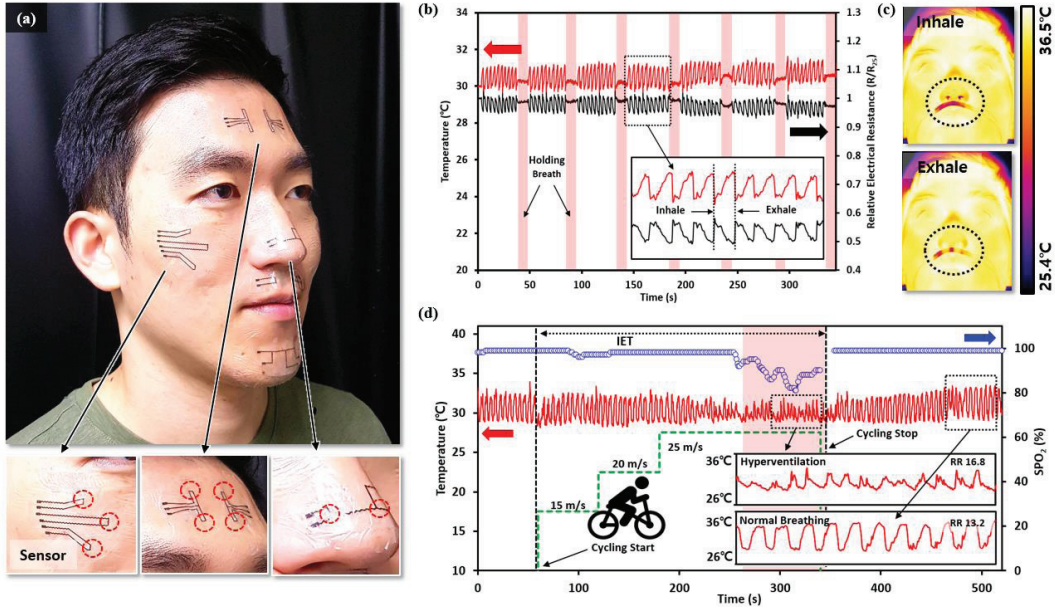


**Figure 10** (a) conformally attachable NiO epidermal temperature sensors attached on various facial positions. (b) Continuous monitoring of respiration temperature (c) Thermal images showing the temperature variation above upper-lip during respiration (d) Real-time monitoring of respiration temperature and SPO<sub>2</sub> change during the incremental exercise test (IET).

Similar to the prosthetic hand, thin and flexible NiO temperature sensor also enable conformal attachment to the various curvature surface of human face. (figure 10a) Furthermore, the design of sensor and electrode can be modified according to the characteristics of the attachment part. Conformal attachment and superior sensing ability are advantageous to the epidermal temperature sensors aiming the accurate

measuring of the thermal signals of the human body metabolism. As shown in figure 10b and 10c, NiO temperature sensor attached above upper-lip can capture temperature change (29.7 °C to 31.2 °C) of the human respiration. To prevent both allergic response of nickel and other stimuli except temperature, the sensor was encapsulated with commercial epidermal tape (Tegaderm, 3M) and attached on the porous PDMS thermal insulating layer (100  $\mu\text{m}$  thickness). Since the sensitivity of the sensor is sufficiently high, it is also possible to measure not only the respiration rate (RR) but also the pattern of respiration. In Figure 10c, we can identify the change of respiration pattern during 3 phase (normal state, incremental exercise and recovery) exercise. 3 minutes after starting the exercise, the respiration temperature variation amplitude decrease 65 % and the respiration rate increases 27 % (16.8 rpm). The increased RR with shallow breathing is the typical symptom of hyperventilation,<sup>43</sup> and lower peripheral capillary oxygen saturation ( $\text{SPO}_2$ ) level also indicates the same result. By the easy modulus matching with human body and accurate capturing of human metabolism, our NiO epidermal temperature sensor has broad usability for someone need real-time monitoring like critically-ill patients, sport players and military combatants.

## Chapter 4. Conclusion

We have presented a method for fabricating highly sensitive and flexible temperature sensor through a simple laser-induced process. Despite its simplicity, the proposed LRS process ensures superior features compared to conventional annealing-involved process. First, selective and sequential laser process allows to use thermally vulnerable yet highly flexible polymer substrate. The thin PET substrate, with nearly negligible mechanical modulus, ensures excellent adhesion between temperature sensor and curved surface. Second, monolithic forming of complete sensor system from a single material, which includes Ni electrode as well as NiO sensing material, provides an align-free and single-step process ensuring improved contact quality. Third, the laser process improves the sensitivity of the NiO temperature sensor without additional treatment. The result of the XRD measurement and the Raman spectroscopy suggests that the laser process effectively inactivate innate nickel vacancies in NiO crystal. Our stoichiometric NiO temperature sensor exhibited the highest temperature-sensitivity near room temperature among reported NTC thermistors. Finally, Through the digital patterning process, it is possible to ensure high design variability of sensor system. The design of sensor system can be easily modified by the CAD program according to the characteristics of the object to be attached. In addition, since a fixed mold or mask is not required, the modified design can be applied immediately.

Based on advantages mentioned above, we presented various applications for artificial skin and epidermal sensor. The 5x5 artificial thermo-receptor array and the

prosthetic hand sensor, which can measure the temperature distribution of a specific area like thermo-receptors of human skin, showed great potential toward practical use in artificial skin. With high temperature-sensitivity, sensors on tip of the artificial finger could detect the temperature variation of the water flowing through the PDMS channel. and the proposed EBT sensor could be utilized in continuous monitoring of EBT for early detection of various diseases related to respiratory system.<sup>7,44</sup>

Through our proposed applications, we have confirmed that the performance of the sensor is sufficient to be used for military robots or combatant vitality monitoring. However, for the practical use in military field, further research on the stability that can be tolerated in the harsh environment should be conducted.



## References

- 1      Someya, T. *et al.* Conformable, flexible, large-area networks of pressure and thermal sensors with organic transistor active matrixes. *PNAS* **102**, 12321-12325, doi:10.1073/pnas.0502392102 (2005).
- 2      Yang, Y. *et al.* An integrated flexible temperature and tactile sensing array using PI-copper films. *Sensor Actuat a-Phys* **143**, 143-153, doi:10.1016/j.sna.2007.10.077 (2008).
- 3      Harada, S. *et al.* Fully Printed Flexible Fingerprint-like Three-Axis Tactile and Slip Force and Temperature Sensors for Artificial Skin. *ACS nano* **8**, 12851-12857, doi:10.1021/nn506293y (2014).
- 4      Tien, N. T. *et al.* A flexible bimodal sensor array for simultaneous sensing of pressure and temperature. *Adv Mater* **26**, 796-804, doi:10.1002/adma.201302869 (2014).
- 5      Kim, J. *et al.* Stretchable silicon nanoribbon electronics for skin prosthesis. *Nat Commun* **5**, 5747, doi:10.1038/ncomms6747 (2014).
- 6      Taylor, N. A., Tipton, M. J. & Kenny, G. P. Considerations for the measurement of core, skin and mean body temperatures. *J Therm Biol* **46**, 72-101, doi:10.1016/j.jtherbio.2014.10.006 (2014).
- 7      Popov, T. A., Kralimarkova, T. Z. & Dimitrov, V. D. Measurement of exhaled breath temperature in science and clinical practice. *Breathe* **8**, 186-192, doi:10.1183/20734735.021811 (2012).
- 8      Trung, T. Q., Ramasundaram, S., Hwang, B. U. & Lee, N. E. An All-Elastomeric Transparent and Stretchable Temperature Sensor for Body-Attachable Wearable Electronics. *Advanced Material* **28**, 502-509, doi:10.1002/adma.201504441 (2016).
- 9      Han, S. *et al.* Battery-free, wireless sensors for full-body pressure and temperature mapping. *Sci Transl Med* **10**,

- doi:10.1126/scitranslmed.aan4950 (2018).
- 10 Feteira, A. Negative Temperature Coefficient Resistance (NTCR) Ceramic Thermistors: An Industrial Perspective. *Journal of the American Ceramic Society* **92**, 967-983, doi:10.1111/j.1551-2916.2009.02990.x (2009).
  - 11 Niesen, T. P. & De Guire, M. R. Review: deposition of ceramic thin films at low temperatures from aqueous solutions. *Solid State Ionics* **151**, 61-68, doi:10.1016/S0167-2738(02)00604-5 (2002).
  - 12 Ko, S. W., Li, J., Podraza, N. J., Dickey, E. C. & Trolier-McKinstry, S. Spin Spray-Deposited Nickel Manganite Thermistor Films For Microbolometer Applications. *Journal of the American Ceramic Society* **94**, 516-523, doi:10.1111/j.1551-2916.2010.04097.x (2011).
  - 13 Chung, J. W., Ko, S. W., Bieri, N. R., Grigoropoulos, C. P. & Poulikakos, D. Conductor microstructures by laser curing of printed gold nanoparticle ink. *Appl Phys Lett* **84**, 801-803, doi:10.1063/1.1644907 (2004).
  - 14 Chung, J. *et al.* Damage-free low temperature pulsed laser printing of gold nanoinks on polymers. *J Heat Trans-T Asme* **127**, 724-732, doi:10.1115/1.1924627 (2005).
  - 15 Yeo, J. *et al.* Next generation non-vacuum, maskless, low temperature nanoparticle ink laser digital direct metal patterning for a large area flexible electronics. *PLoS One* **7**, e42315, doi:10.1371/journal.pone.0042315 (2012).
  - 16 Hong, S. *et al.* Nonvacuum, maskless fabrication of a flexible metal grid transparent conductor by low-temperature selective laser sintering of nanoparticle ink. *ACS nano* **7**, 5024-5031, doi:10.1021/nn400432z (2013).
  - 17 Kang, B., Han, S., Kim, J., Ko, S. & Yang, M. One-Step Fabrication of Copper Electrode by Laser-Induced Direct Local Reduction and Agglomeration of Copper Oxide Nanoparticle. *J Phys Chem C* **115**, 23664-23670, doi:10.1021/jp205281a (2011).
  - 18 Lee, D., Paeng, D., Park, H. K. & Grigoropoulos, C. P. Vacuum-free,

- maskless patterning of Ni electrodes by laser reductive sintering of NiO nanoparticle ink and its application to transparent conductors. *ACS nano* **8**, 9807-9814, doi:10.1021/nn503383z (2014).
- 19 Lee, H. & Yang, M. Effect of solvent and PVP on electrode conductivity in laser-induced reduction process. *Appl Phys a-Mater* **119**, 317-323, doi:10.1007/s00339-014-8970-6 (2015).
  - 20 Paeng, D. *et al.* Laser-Induced Reductive Sintering of Nickel Oxide Nanoparticles under Ambient Conditions. *J Phys Chem C* **119**, 6363-6372, doi:10.1021/jp512776p (2015).
  - 21 Huang, C. C., Kao, Z. K. & Liao, Y. C. Flexible Miniaturized Nickel Oxide Thermistor Arrays via Inkjet Printing Technology. *ACS Appl Mater Interfaces* **5**, 12954-12959, doi:10.1021/am404872j (2013).
  - 22 Umadevi, P. & Nagendra, C. L. Preparation and characterisation of transition metal oxide micro-thermistors and their application to immersed thermistor bolometer infrared detectors. *Sensors and Actuators A: Physical* **96**, 114-124, doi:10.1016/S0924-4247(01)00776-2 (2002).
  - 23 Fang, D. L. *et al.* Preparation of ultra-fine nickel manganite powders and ceramics by a solid-state coordination reaction. *Journal of the American Ceramic Society* **89**, 230-235, doi:10.1111/j.1551-2916.2005.00666.x (2006).
  - 24 Fang, D. L., Lee, C. G. & Koo, B. H. Preparation of ultra-fine FeNiMnO<sub>4</sub> powders and ceramics by a solid-state coordination reaction. *Met Mater-Int* **13**, 165-170, doi:10.1007/Bf03027568 (2007).
  - 25 Ryu, J. *et al.* Highly Dense and Nanograined NiMn<sub>2</sub>O<sub>4</sub> Negative Temperature coefficient Thermistor Thick Films Fabricated by Aerosol-Deposition. *Journal of the American Ceramic Society* **92**, 3084-3087, doi:10.1111/j.1551-2916.2009.03300.x (2009).
  - 26 Schulze, H., Li, J., Dickey, E. C. & Troler-McKinstry, S. Synthesis, Phase

- Characterization, and Properties of Chemical Solution-Deposited Nickel Manganite Thermistor Thin Films. *Journal of the American Ceramic Society* **92**, 738-744, doi:10.1111/j.1551-2916.2009.02944.x (2009).
- 27 Kang, J. E. *et al.* LaNiO<sub>3</sub> conducting particle dispersed NiMn<sub>2</sub>O<sub>4</sub> nanocomposite NTC thermistor thick films by aerosol deposition. *J Alloy Compd* **534**, 70-73, doi:10.1016/j.jallcom.2012.04.038 (2012).
  - 28 Aleksic, O. S. *et al.* Preparation and characterization of Cu and Zn modified nickel manganite NTC powders and thick film thermistors. *Materials Science and Engineering: B* **178**, 202-210, doi:10.1016/j.mseb.2012.11.003 (2013).
  - 29 Ma, C., Liu, Y., Lu, Y. & Qian, H. Preparation and electrical properties of Ni<sub>0.6</sub>Mn<sub>2.4-x</sub>Ti<sub>x</sub>O<sub>4</sub> NTC ceramics. *J Alloy Compd* **650**, 931-935, doi:10.1016/j.jallcom.2015.08.077 (2015).
  - 30 Le, D. *et al.* Characterization of ternary (Ni,Co,Mn)<sub>3</sub>O<sub>4</sub> thin films for microbolometer applications. *J Alloy Compd* **650**, 415-420, doi:10.1016/j.jallcom.2015.07.236 (2015).
  - 31 Wang, C., Hong, G. Y., Li, K. M. & Young, H. T. A Miniaturized Nickel Oxide Thermistor via Aerosol Jet Technology. *Sensors* **17**, 2602, doi:10.3390/s17112602 (2017).
  - 32 Park, J. Microstructural and electrical properties of Y<sub>0.2</sub>Al<sub>0.1</sub>Mn<sub>0.27-x</sub>Fe<sub>0.16</sub>Ni<sub>0.27-x</sub>(Cr<sub>2x</sub>)O<sub>y</sub> for NTC thermistors. *Ceramics International* **41**, 6386-6390, doi:10.1016/j.ceramint.2015.01.075 (2015).
  - 33 Xia, J., Zhao, Q., Chang, A. & Zhang, B. Synthesis and properties of Mn<sub>1.05-y</sub>Co<sub>1.95-x-z</sub>W<sub>x</sub>Ni<sub>x</sub>Mg<sub>y</sub>Al<sub>z</sub>Fe<sub>w</sub>O<sub>4</sub> NTC ceramic by co-precipitation method. *J Alloy Compd* **646**, 249-256, doi:10.1016/j.jallcom.2015.06.073 (2015).
  - 34 Maslar, J. E., Hurst, W. S., Bowers, W. J., Hendricks, J. H. & Aquino, M. I. In situ Raman spectroscopic investigation of nickel hydrothermal corrosion. *Corrosion* **58**, 225-231, doi:10.5006/1.3279873 (2002).

- 35 Mironova-Ulmane, N., Kuzmin, A., Sildos, I. & Pars, M. Polarisation dependent Raman study of single-crystal nickel oxide. *Central European Journal of Physics* **9**, 1096-1099, doi:10.2478/s11534-010-0130-9 (2011).
- 36 Jang, W. L., Lu, Y. M., Hwang, W. S., Hsiung, T. L. & Wang, H. P. Point defects in sputtered NiO films. *Appl Phys Lett* **94**, 062103, doi:10.1063/1.3081025 (2009).
- 37 Kim, D. S. & Lee, H. C. Nickel vacancy behavior in the electrical conductance of nonstoichiometric nickel oxide film. *J Appl Phys* **112**, 034504, doi:10.1063/1.4742993 (2012).
- 38 Seo, S. *et al.* Reproducible resistance switching in polycrystalline NiO films. *Appl Phys Lett* **85**, 5655-5657, doi:10.1063/1.1831560 (2004).
- 39 Kaneko, S. *et al.* Large constriction of lattice constant in epitaxial magnesium oxide thin film: Effect of point defects on lattice constant. *J Appl Phys* **107**, 073523, doi:10.1063/1.3361482 (2010).
- 40 Adler, D. & Feinleib, J. Electrical and optical properties of narrow-band materials. *Phys Rev B-Solid St* **2**, 3112-3134, doi:DOI 10.1103/PhysRevB.2.3112 (1970).
- 41 Biju, V. & Abdul Khadar, M. DC conductivity of consolidated nanoparticles of NiO. *Materials Research Bulletin* **36**, 21-33, doi:10.1016/S0025-5408(01)00488-3 (2001).
- 42 Gardner, E., Martin, J., Jessell, T., Kandel, E. & Schwartz, J. Principles of neural science. *McGraw-Hill, New York*, 451-471 (2000).
- 43 Arbus, G. S., Hebert, L. A., Levesque, P. R., Etsten, B. E. & Schwartz, W. B. Characterization and Clinical Application of the Significance Band for Acute Respiratory Alkalosis. *N Engl J Med* **280**, 117-123, doi:10.1056/nejm196901162800301 (1969).
- 44 Folke, M., Cernerud, L., Ekstrom, M. & Hok, B. Critical review of non-invasive respiratory monitoring in medical care. *Med Biol Eng Comput* **41**, 377-383, doi:10.1007/bf02348078 (2003).

## Abstract in Korean

### Fabrication of Highly Sensitive Flexible Nickel Oxide NTC Temperature Sensor using Monolithic Digital Laser Patterning Process

정 부 성 (Buseong Jeong)

기계항공공학부 기계공학전공 (Mechanical Engineering)

Seoul National University

높은 온도 민감도와 단순한 구조에도 불구하고 NTC 서미스터는 높은 공정 온도로 인해 유연한 기판과의 호환성이 낮아 인공 피부나 박막 온도 센서에 제한적으로만 활용되어 왔다. 이러한 문제점을 해결하기 위해 본 논문에서는 상온 조건에서 니켈 전극과 니켈옥사이드 센서를 단일 단계의 모노리딕 공정으로 제작 가능하고, 선별적이고 순차적인 열처리가 가능한 레이저 디지털 패터닝 공정을 제시하였다. 모노리딕 공정을 통해 제작된 “니켈-니켈산화물-니켈” 연결을 가진 NTC 서미스터는 기존 학계에 보고된 NTC 서미스터 중 가장 높은 온도 민감도 ( $TCR -9.2\%/^{\circ}C$ ,  $B=8162\text{ K at }25^{\circ}C$ )를 가진다. 물리적 분석을 통해 이러한 우수한 온도 민감도는 레이저 공정의 특별한 열적 활성화 과정에 기인한다는 것을 확인 하였다. 우수한 온도 민감도와 기판에 가해지는 열 피해가 적다는 레이저 공정의 장점을 통해 유연한 온도 센서 어레이와 균등한 부착이 가능한 온도 센서를 개발하였다. 이러한 성과를 통해 인공 피부와 박막 온도 센서로의 활용 가능성을 확인하였고, 이를 군사 분야에서 활용 시 효율적인 작전수행이 가능할 것이라 판단된다.

**Keyword:** 레이저 디지털 패터닝, 니켈옥사이드, 온도 센서, 인공피부, 박막센서

**Student Number:** 2017-24786